Starlight beneath the waves : in search of TeV photon emission from Gamma-Ray Bursts with the ANTARES Neutrino Telescope

Laksmana-Astraatmadja, T.

Part II

Detector & simulations

6 The ANTARES neutrino telescope

On May 29th 2008, the 12th line of the ANTARES neutrino telescope was put in operation thus completing the construction which has begun in 2006 (Ageron et al., 2011). This makes ANTARES the largest neutrino telescope in the northern hemisphere and the second largest neutrino telescope in the world.

Due to the location at the bottom of the sea, at a depth of 2475 m, many technical challenges had to be met to overcome the problems that can arise from deep-sea environments. Following a discussion on the basic detection principle of a neutrino telescope, this Chapter will discuss the architecture of the ANTARES telescope and the method to reconstruct muon tracks that pass through the detector.

6.1 Čerenkov photons

When a charged particle such as a muon traverses a medium with velocity β greater than the speed of light in that medium, $u = 1/n$, where n is the refraction index of the medium, an electromagnetic shock-wave will be generated along the trajectory of the particle (Figure 6.1). This shock-wave is in the form of coherent radiation of photons emitted at a characteristic angle θ_C with respect to the particle's trajectory, which is determined by (Čerenkov, 1937)

$$\cos\theta_C = \frac{1}{\beta n}, \quad \beta > \frac{1}{n}. \tag{6.1}$$

Here velocities β and u are expressed in fractions of the speed of light in vacuum c.

For relativistic particles with velocities $\beta \simeq 1$ traversing through water ($n = 1.33$), the angle is $\theta_C \simeq 41.2°$.

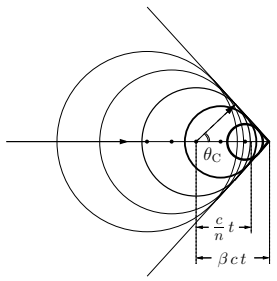

Figure 6.1: An illustration of the Čerenkov wavefront of the photons emitted at an angle θ_C. Figure reproduced from Lim (2011).

This radiation is named after Pavel Čerenkov who first noticed a very weak visible radiation from pure liquids under the influence of γ-rays in his experiments (Čerenkov, 1934, 1937). This happened because the electromagnetic field of the traversing particle distorts the atoms such that they will be polarized toward the trajectory of the particle. The atoms will then emit photons as they return to equilibrium (Jelley, 1958). The number of photons

emitted per unit wavelength per unit unit distance is

$$\frac{dN}{d\lambda dx} = \frac{2\pi\alpha Z^2}{\lambda^2}\left(1 - \frac{1}{n^2\beta^2}\right), \tag{6.2}$$

where α is the fine structure constant, Z is the electric charge of the moving particle, and λ is the wavelength of the photons. If we integrate Equation 6.2 over λ, we obtain the number of photons emitted within a range of wavelength between λ_1 and λ_2 (Jelley, 1958):

$$\frac{dN}{dx} = 2\pi\alpha Z^2\left(\frac{1}{\lambda_1} - \frac{1}{\lambda_2}\right)\left(1 - \frac{1}{n^2\beta^2}\right). \tag{6.3}$$

Thus for a relativistic muon with $\beta \simeq 1$ in water, approximately 30 000 photons in the visible spectrum ($350\ \text{nm} \leq \lambda \leq 750\ \text{nm}$) are emitted per meter.

6.2 *Detection principle of a neutrino telescope*

When a cosmic neutrino passes through the Earth, it may interact via the charged current interactions to produce a muon that could come out of the other side of the Earth (Figure 6.2). The muon will travel in the same direction as the neutrino with minor deviation. An upgoing track will confirm the neutrino origin of the muon since no other known particles can traverse the entire Earth.

In order to detect the faint Čerenkov light, no other source of light—such as sunlight or manmade light source—should be detected. The detector must also be deep enough to veto as much atmospheric muons as possible. Atmospheric muons are muons resulting from the interaction of cosmic rays with the atmosphere. They can have sufficient energy to penetrate great depths, but they should be detected as downgoing muon tracks (Figure 6.2). These muons will constitute a background if the direction is not accurately reconstructed. Another background is due to atmospheric neutrinos, which are also the result of cosmic-ray interactions with the atmosphere. They are indistinguishable from cosmic neutrinos.

The wavefront of the Čerenkov photons is a cone. To detect these photons, a neutrino telescope comprises a three-dimensional

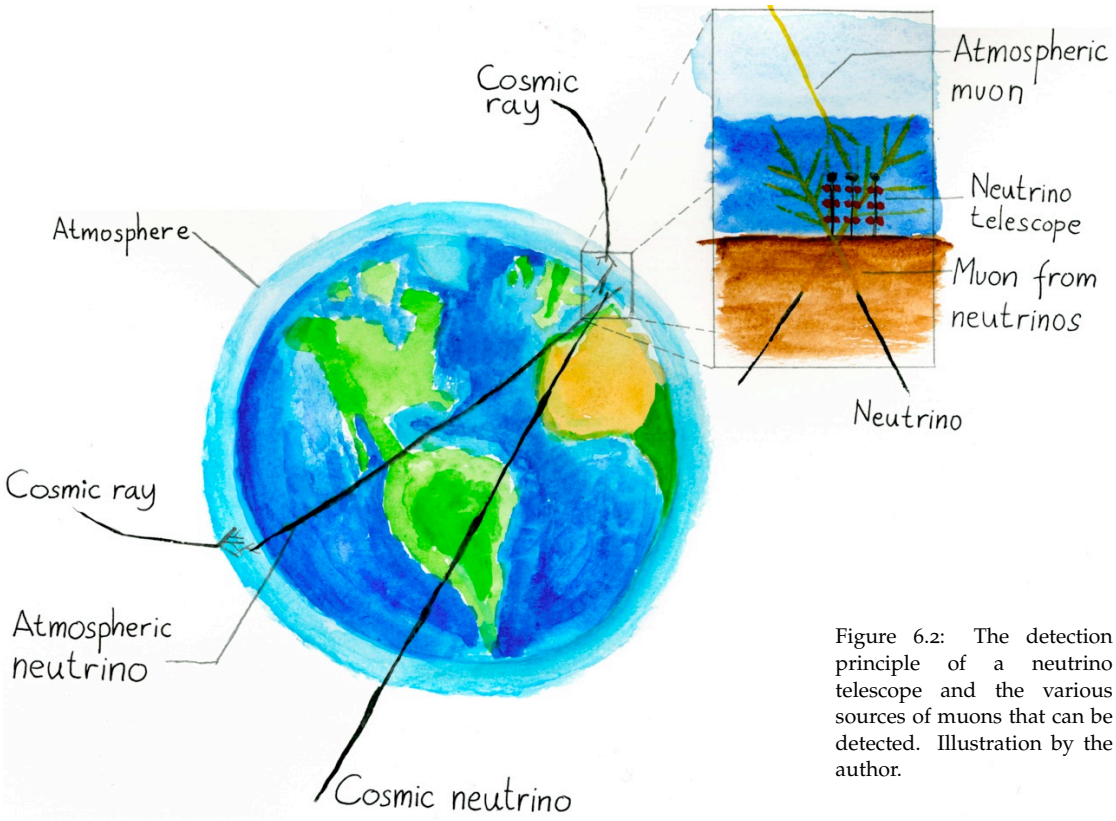

Figure 6.2: The detection principle of a neutrino telescope and the various sources of muons that can be detected. Illustration by the author.

arrangement of light-sensitive detectors, usually photomultiplier tubes (PMT). The PMTs record the arrival time and amplitude of the Čerenkov photons. For an underwater detector such as ANTARES, the PMTs are housed in a transparent pressure casing to protect the PMTs and its electronic instruments against the hostile environment of the deep sea.

6.3 *The ANTARES detector*

The site of ANTARES is approximately 40 km to the southeast of Toulon, south of France (Figure 6.3). The control station of ANTARES is located at La Seyne-sur-Mer, a commune located at the west of Toulon. Power to the detector and data from the detector

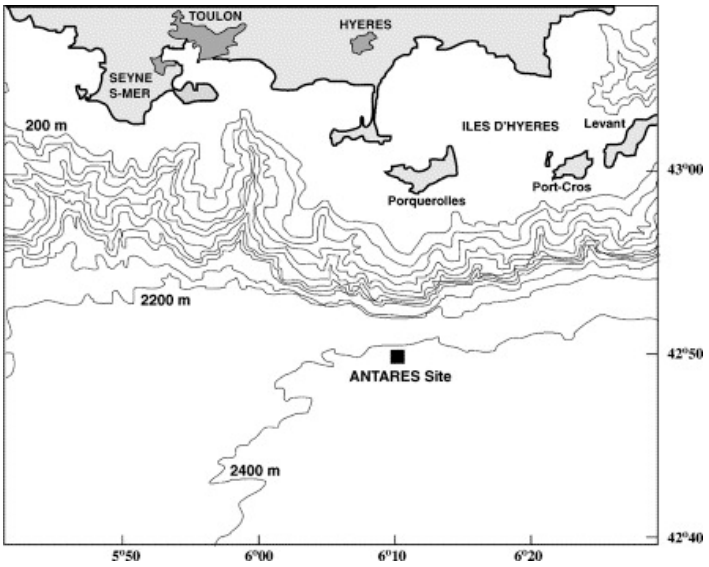

Figure 6.3: The depth contour of the Mediterranean Sea around the site of ANTARES. ANTARES is located approximately 40 km off the coast of Toulon, south of France, at a depth of 2475 m.

are transmitted through an electro-optical cable that connects the detector to the control station on the shore.

ANTARES is located on the seabed at a depth of 2475 m. All components of the detector must then be able to withstand a hydrostatic pressure between 200 and 256 bar and resist the corrosion of sea water for a minimum detector lifetime of 10 years (Ageron et al., 2011). The following subsections will give a brief description of the most important components of ANTARES. A more complete overview is given in Ageron et al. (2011).

6.3.1 The Optical Module (OM)

The basic element of ANTARES is a glass sphere with a PMT inside, called optical module (OM), shown in Figure 6.4. The glass sphere has a diameter of 43 cm and 15 mm thickness. The material is a transparent Vitrovex® glass sphere with >95% transmission for light with wavelength above 350 nm. The glass sphere contains a PMT and a magnetic shield, kept in place by an optical gel. The gel is a two-component silicon rubber with elasticity soft enough absorb the sphere diameter reduction by the deep sea pressure and yet stiff enough to hold the PMT in place (Amram et al., 2002).

The photomultiplier tube is the Hamamatsu 10" PMT model

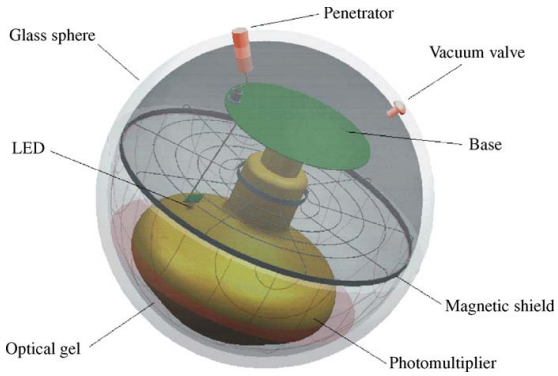

Figure 6.4: *Left:* Schematic view of an ANTARES optical module (OM). *Right:* A Hamamatsu R7081-20 10″ photomultiplier tube. Figures reproduced from Amram et al. (2002).

R7801-20 (Figure 6.4, right). It is a large hemispherical PMT of 25 cm in diameter and an effective sensitive area of 440 cm^2. It is sensive to photons with wavelength in the visible spectrum between 300–600 nm, with peak quantum efficiency (QE) of 23% at wavelength of 350–450 nm. At a voltage of 1760 V the PMT has a nominal gain of 5×10^7. The accuracy of the measurement of the arrival time of a photon at the photocathode is determined by the Transit Time Spread (TTS). From the measurements of 912 PMTs, the TTS is found to be 2.79 ± 0.15 ns and the dark noise rate to be 1.88 ± 1.08 kHz (Aguilar et al., 2005a).

The PMT is surrounded by a mesh of μ-metal wires to minimize the influence of the Earth's magnetic field. The size of the wire mesh is 68×68 mm^2 with a wire diameter of 1.08 mm, resulting in a shadowing effect of less than 4% of the photocathode area while reducing the magnetic field effects by a factor of 2.5 (Amram et al., 2002).

μ-metal is a nickel-iron alloy that has a very-high magnetic permeability for low-intensity magnetic fields.

The high voltage system to power the PMT adopts the Cockcroft–Walton scheme (Cockcroft & Walton, 1932) to limit the power consumption to less than 300 mW. This is a factor 10 reduction compared to standard converters and passive dividers (Amram et al., 2002). The system has two independent high-voltage chains. The first chain produces a constant focusing voltage (800 V) to be applied between photocathode and first dynode, while the second

chain gives the amplification voltage which can be adjusted from 400 to 1600 V by an external DC voltage (Ageron et al., 2011). A 48 V DC power supply powers the HV generator.

The OM is also equipped with a LED system used for internal calibration, especially for the calibration of the TTS. This system consists of a fast blue light-emitting diode (LED) with peak intensity around 470 nm. The LED is glued on the back of the PMT to optimally illuminate the photocathode through the aluminium coating of the tube (Amram et al., 2002). The LED is activated by an externally-driven pulser circuit.

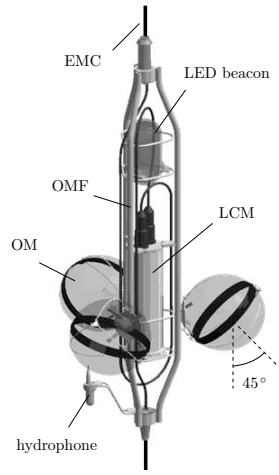

Figure 6.5: Schematic view of an ANTARES floor and its component. Figure reproduced from Lim (2011).

6.3.2 *Floors, sectors, and detector lines*

The optical modules are grouped together in triplets to form a floor or storey (Figure 6.5). The PMTs point downwards at 45° angle relative to the vertical to optimize photon collection from upgoing muon tracks. The frame that hold them together, the optical module frame (OMF), also holds the local control module (LCM). The LCM is a Titanium cylinder housing the readout electronics. The OMF also supports various instruments for calibration and monitoring.

Floors are connected with each other by an electromechanical cable (EMC). The EMC contains 21 optical fibres for data transmission as well as 9 electrical conductors for power distribution. The distance between each floors is 14.5 m. Five connected floors make up a sector and a sector is an individual unit as far as power supply and data transmission are concerned. In each sector, one of the five LCMs is a Master LCM (MLCM) that manages data transfer between all LCMs and in the sector and the shore.

A single detector line (Figure 6.6) consists of 25 floors (or 5 sectors) linked together by the EMC. The line is anchored to the seabed by a Bottom String Structure (BSS). The BSS also allows line recovery by means of two parts: an unrecoverable deadweight on the seabed and a recoverable part on top of it, which are connected together by a release system remotely controlled by acoustic signals (Ageron et al., 2011). The BSS also contains a String Control Module (SCM) and a String Power Module (SPM). The SCM contains electronics that manages the data transmission between sectors in the line and the shore. The SPM provides indi-

vidual power supplies for all sectors in the line.

The distance between the seabed to the lowest floor of each line is 100 m, to maximize the development of the Čerenkov cone for upgoing muon tracks. At the top of each line, a buoy is placed to keep the line vertical.

THE FULL ANTARES detector (Figures 6.7) consists of 12 detector lines distributed in an octagonal configuration and a dedicated instrumentation line (IL). The instrumentation line is equipped with instruments dedicated for acoustic neutrino detection (Aguilar et al., 2011b) and environmental monitoring. The last line, Line 12, contains only 20 floors. The lines are separated by an average distance of ∼60 m. The BSS of each line is connected to the junction box (JB) which is the main distribution point of data and power supply between the detector lines and the shore. The junction box is connected to the shore by a ∼40 km main electro-optical cable (MEOC).

Altogether, the 885 OMs in the 12 detector lines that comprise ANTARES cover an instrumented volume of approximately 1.1×10^7 m^3.

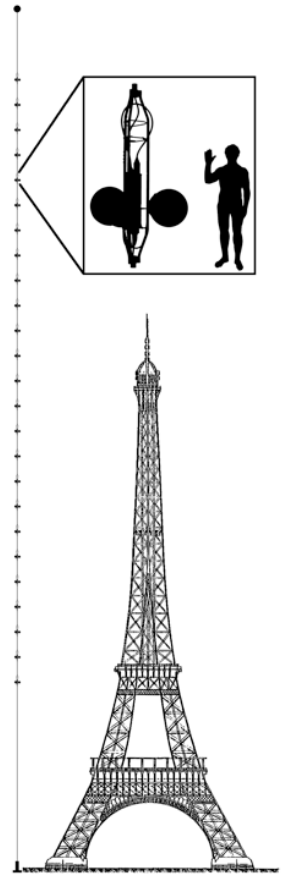

Figure 6.6: A schematic view of an ANTARES detector line and its floors, compared with the Eiffel Tower (324 m). Also shown at the inset is the comparison of an ANTARES floor to the *Pioneer* plaque man (168 cm). Figure courtesy of Guillard (2011).

6.4 *Data acquisition (DAQ) system*

THE MAIN purpose of the data acquisition (DAQ) system is to convert the analogue signals from the PMTs into a format suitable for physics analysis. This process consists of several steps: The preparation for data taking, digitization of the analogue signals from the PMTs, transporting the data to shore, filtering the physics signals from backgrounds, storing and archival (Aguilar et al., 2007). Some of these aspects will be discussed below.

6.4.1 *Signal digitization*

WHEN A photon hits the photocathode of a PMT, an electron may be emitted through photoelectric effect. The electron is then accelerated through the dynode structure of the PMT and multiplied. The quantum efficiency of the PMT determines whether a photon in a certain wavelength could be detected.

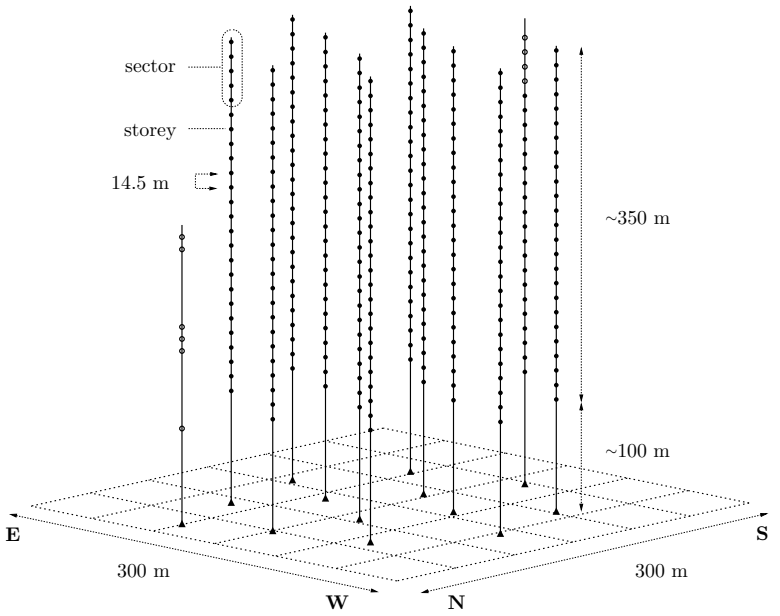

Figure 6.7: A schematic view of the full ANTARES detector, which consists of 12 detector lines of 25 floors each, and an instrumentation line (IL) of 6 storeys. Line 12 has only 20 floors. Figure reproduced from Lim (2011).

Digitization of the analogue signal occurs when the amplitude of the signal exceeds a predetermined voltage threshold. The threshold is typically set to a 0.3 of the single photoelectron signal, to suppress the PMT dark current. Signal digitization is performed by a custom-made front-end chip called the Analogue Ring Sampler (ARS). The ARS timestamps the signal when it crosses the threshold. The time is defined with respect to a reference time provided by a local clock which is synchronized with the onshore master clock. The timing resoluting is better than 0.4 ns (Aguilar et al., 2010).

The change of the analogue signals is measured with an 8-bit Analogue-to-Digital Converters (ADC), with an integration gate typically set to about 35 ns to minimize the contribution of electronic noise (Aguilar et al., 2007). A dead time of ∼250 ns is introduced when the ARS is processing signals. Therefore two ARS chips are used in order to minimizes this dead time. The minimum time difference between two consecutive hits in the same PMT can thus be as low as 38 ns (Aguilar et al., 2010).

The combined charge and time information of a PMT signal is called a level zero (L0) hit. All 6 ARS chips in an LCM are read-out by a Field Programmable Gate Array (FPGA) that arranges the hits produced in a preset time window into a dataframe, and buffers these in a 64 MB Synchronous Dynamic Random Access Memory (SDRAM). The complete set of dataframes from all ARSs corresponding to the same time window is called a time slice.

6.4.2 *Data transfer, storage and filtering*

During data taking, all signals recorded by the PMTs and digitized by the ARS chips are transported to the shore station without any selection. This concept is known as the all-data-to-shore concept. All raw data are then available on shore in which further analysis can be applied.

Each LCM contains a CPU connected to the onshore computer farm through the main electro-optical cable. The buffered data stored in the SDRAM are sent as single packet to shore using TCP/IP (Aguilar et al., 2007). Each LCM CPU is connected to the MLCM through a bidirectional Fast Ethernet link of 100 Mb/s. In the MLCM, these links are multiplexed using an Ethernet switch into two unidirectional 1 Gb/s links, one for incoming control signals and one for outgoing data.

Data transport between the detector and the shore station employs the dense wavelength division multiplexing (DWDM). Multiple wavelength are used to transmit different streams of data along a single fibre (Aguilar et al., 2007).

As a consequence of the all-data-to-shore concept, the rate of data is typically at 0.3–0.5 Gb/s (Aguilar et al., 2007). The vast majority of these data are due to the optical background in the sea. A filtering system must be employed to reduce the demand for data storage. A computer farm in the shore station is used for this purpose. The algorithms implemented are designed to search for a physics signal by looking for space-time correlations between hits. The algorithm look for a set of causally-connected hits. If such event is found, all hits during a preset time window are stored.

6.5 Calibrations

THERE are various calibrations performed to operate the detector optimally: The time calibration is necessary to precisely determine the arrival time of the Čerenkov photons at each PMT. Because of sea currents and the flexibility of the electromechanical cables, the detector lines can sway sideways and thus displace the position of each PMT relative to the vertical. Position calibration is performed to determine the accurate location of all PMTs at any given time.

A precise measurement of the photon arrival time and the position of each PMTs allows tracks to be reconstructed with an accurate angular resolution, which is expected to be $\lesssim 0.3^\circ$ for muons of energies above 10 TeV (Ageron et al., 2007). The charge calibration is used to convert the data into units photoelectrons.

6.5.1 Time calibration

THE RELATIVE arrival times of the Čerenkov photons between PMTs are essential for an accurate reconstruction of the muon direction. The difference of each local clock relative to the onshore master clock thus has to be known. The time resolution of the clock is limited by the transit time spread (TTS) of the signal in the PMTs and by the scattering and chromatic dispersion of light in seawater which typically has $\sigma \sim 1.5$ ns (Aguilar et al., 2005b).

Time calibration should reach a precision below the nanosecond level. Several complementary, independent calibration system are implemented to this end.

The internal clock calibration system sends signals between the onshore master clock and the local clock in each LCMs. The time offset between all LCM clocks can be measured by recording the time delays of the return signals of each floor relative to the original clock signal emission time. A resolution of $\sim$0.1 ns is obtained from measurements in real conditions (Aguilar et al., 2011a).

The blue LED inside each OMs is used to measure the relative variation of the PMT transit time. Using this method, the path traversed by the signal from the PMT photocathode up to readout electronics can be monitored. Over an eight month period, the variation of the transit time is found to be less than $\sim$0.2 ns (Aguilar et al., 2011a).

The optical beacon system allows the relative time calibration of different OMs to be determined as well as the influence of water properties on the light propagation to be monitored (Ageron et al., 2007). The optical beacon system consists of a series of pulsed light sources distributed throughout the detector. An LED beacon is composed of several LEDs, pulsed by dedicated electronic circuits. Four blue LED (470 nm) beacons are located in every line of the detector at floors 2, 9, 15, and 21 (counted from bottom to top), and two green (532 nm) laser beacons are located on the BSS of lines 7 and 8 (Aguilar et al., 2011a). Once per week a time calibration is done using the LED and laser beacons.

Calibration using the optical beacon system yield a time resolution of $\sim$0.5 ns. The time resolution is thus dominated by contributions from the transit time spread of the PMT, and the contributions from the scattering and chromatic dispersion of light in water (Aguilar et al., 2011a).

Absolute timing is performed by synchronizing the onshore master clock with the Global Positioning System (GPS) time, which provides a time accuracy of $\sim$100 ns (Aguilar et al., 2011a).

6.5.2 *Position calibration*

The sway of the detector lines due to sea currents is measured by two independent systems: an acoustic positioning system and a tiltmeter-compass system (Ardid, 2009).

A High Frequency Long Baseline (HFLBL) acoustic system is used to determine the three-dimensional position of hydrophones along a detector line. The positions are obtained by triangulation from emitters anchored in the base of the line and autonomous transporders on the sea floor. This method has an accuracy of 10 cm.

The tiltmeter-compass system gives the local measurements of tilts (roll, pitch) and heading of storeys. The system has a measurement accuracy of 0.2° in tilt and 1° in heading. The measurements of the tilt and heading of each detector line is performed every 2 minutes.

The swaying of the detector line is reconstructed using a global χ^2 fit of a line shape model to the data. The line shape model is then employed to calculate the position of all OMs at any given

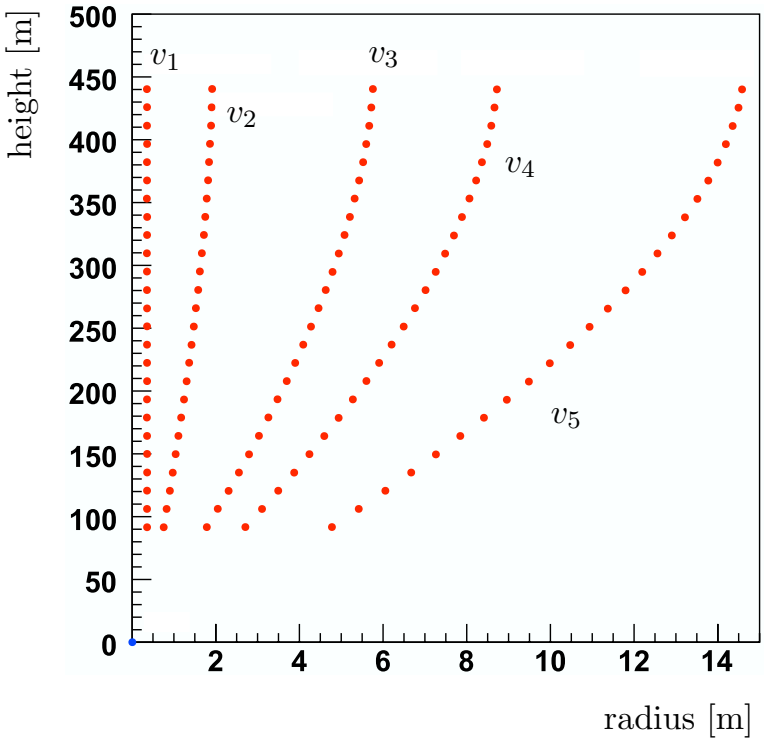

Figure 6.8: The shape of a detector line due to sea current. The swaying is shown for various sea current velocities: $v_1 = 0.01$ cm/s, $v_2 = 7$ cm/s, $v_3 = 12.6$ cm/s, $v_4 = 16$ cm/s, and $v_5 = 20$ cm/s. The horizontal scale is exaggerated for illustration purpose. Figure reproduced from Fritsch (2010).

time, relative to the position of the BSS. The absolute position of the BSS itself is determined during the deployment of the BSS with a remotely operated vehicle (ROV). This is performed by acoustic positioning of the ROV and knowing the GPS location of the ship at the surface. The reconstructed detector line shape due to various values of sea current velocities is shown in Figure 6.8.

6.6 *Triggering and track reconstruction*

The majority of the data taken by ANTARES will come from random backgrounds due to the decay of the radioactive Potassium isotope ^{40}K, and bioluminescence.

The decay of ^{40}K will introduce a continuous baseline rate of ∼35 kHz (Figure 6.9) in the measurement of photon rate by the PMTs (Amram et al., 2000). Bioluminescence, which is caused

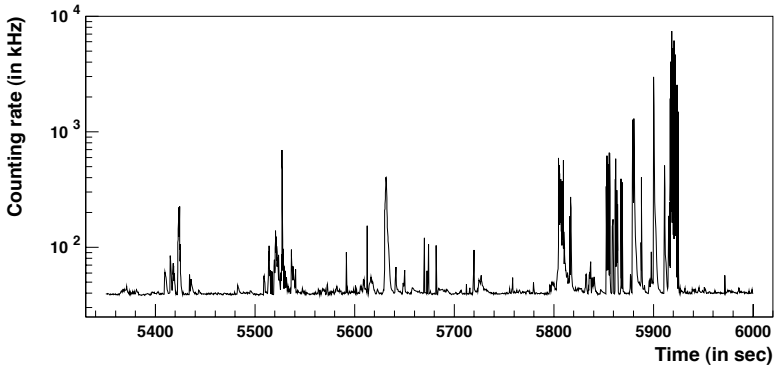

Figure 6.9: A typical measurement of the photon counting rate at 0.3 pe level. A continuous baseline rate of ∼35 kHz can be observed here, which is due to the ^{40}K decay. We can also see an occasional burst of photon rate which is due to bioluminescence. Figure reproduced from Amram et al. (2000).

by marine life, will give rise to bursts with rates up to several orders of magnitude above the baseline rate. Long-term observations show that these burst due to bioluminescence have seasonal variations that correlate with the sea current.

A reduction of this background noise can be obtained by searching for hits within a 20 ns window in PMTs of the same floor or single hits with an amplitude higher than 3 pe. Hits satisfying these criteria are called level one (L1) hits. By searching for L1 hits satisfying the causality relation one can reduce the background rate by a factor of $\sim 10^4$ (de Jong, 2005).

6.6.1 *Causality relation*

PHOTON hits due to the emission of Čerenkov radiation from a muon track should be causally related in space-time. In Figure 6.10 the track of a muon passing through a part of the detector is depicted. Consider a pair of hits detected in PMT$_i$ and PMT$_j$ respectively at time t_i and time t_j. If we assume that both hits are Čerenkov photons emitted by the same muon, the time of the hits and the distance between the PMTs must then satisfy the causality relation

$$|t_i - t_j| = r_{ij}\frac{n}{c}, \tag{6.4}$$

where r_{ij} is the distance between the two PMTs, n is the refractive index of seawater, and c is the speed of light (Figure 6.10). This Equation can be used to look for a cluster of hits. If the cluster

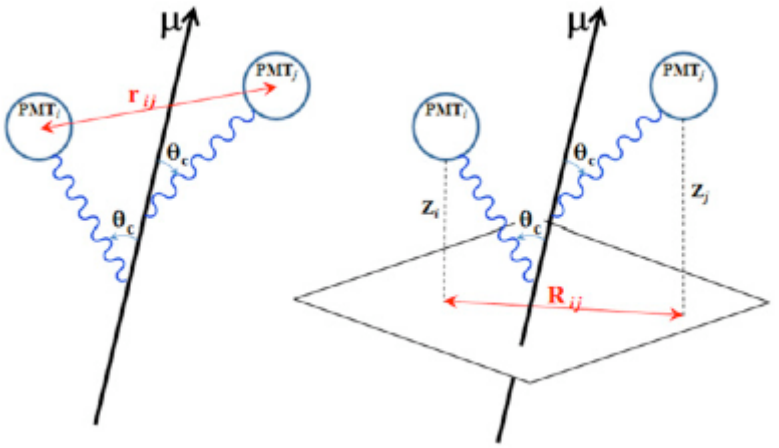

Figure 6.10: *Left:* Definitions employed in the causality criterion. *Right:* Definitions employed in a directional trigger. Figure reproduced from Ageron et al. (2011).

contains at least 5 L1 hits or a local cluster of neighbouring L1 hits, then the event will stored.

A directional trigger can be applied which includes a scan over a number of directions. Two hits can be considered to come from the same muon track if they satisfy the direction-specific causality relation

$$(z_i - z_j) - R_{ij} \tan\theta_C \leq c(t_i - t_j) \leq (z_i - z_j) + R_{ij} \tan\theta_C, \qquad (6.5)$$

where $z_{i,j}$ refers to the positions of PMT i, j along the muon direction, R_{ij} is the distance between the two PMTs in the plane perpendicular to the muon direction, and θ_C is the Čerenkov angle in water. If a cluster contains at least 5 L1 hits within $R_{ij} \leq 90$ m, the event will be triggered.

6.6.2 *Onshore filtering system and the GRB Coordinates Network (GCN)*

The PC farm that comprises the onshore filtering system is also linked to the GRB Coordinates Network (GCN). Whenever an alert from GCN is received, all raw data currently being processed are immediately saved to disk. The data stored in memory, which were taken before the alert is received, are also saved to disk. This is possible because the data filtering PCs serve also as a buffering system that delay the filtering process and store the raw data

memory as long as possible. This allows us to save the raw data up to 4 minutes taken before the alert was received (Bouwhuis, 2005). It is possible to store all the raw data up to 3 minutes after the alert is received, this depends on the size of the raw data itself. This linking of onshore filtering system to GCN alert system allows the sensitivity of ANTARES to transient sources such as GRBs or X-ray flares to be maximized.

6.6.3 *Track reconstruction*

THE GOAL of track reconstruction is to obtain the position and direction of the muon track based on the recorded photon hits. The trajectory of the muon can be expressed by the normalized direction $\mathbf{d} \equiv (d_x, d_y, d_z)$, the position $\mathbf{p} \equiv (p_x, p_y, p_z)$ at a fixed time t_0. We can also express the direction in terms of azimuth ϕ and zenith distance θ, i.e. $\mathbf{d} = (\sin\theta\cos\phi, \sin\theta\sin\phi, \cos\theta)$, which explicitly reduces the number of directional parameters to two. There are thus five independent parameters that we seek.

The reconstruction algorithm is performed in four consecutive procedures, in which the final procedure gives the most accurate result but requires an *a priori* estimate of the track parameters that should be close to the true values (Heijboer, 2004).

In general, the fitting is based on the time residuals of the recorded hits:

$$r_i = t_i - t_{i,\text{th}}, \tag{6.6}$$

where t_i is recorded time of a hit and $t_{i,\text{th}}$ is the theoretical time of hit should it comes from a Čerenkov photon, given the track parameters.

To calculate the theoretical time of hit $t_{i,\text{th}}$ we must first know the distance between the track and the PMT in which it is recorded. In Figure 6.11, the geometry is described. Let us first define $\mathbf{v} = \mathbf{q} - \mathbf{p}$. We can project $\mathbf{v}$ to the track to obtain $\|\mathbf{l}\| = \mathbf{v} \cdot \mathbf{d}$. The length of vector $\mathbf{k}$ can then be computed by

$$\|\mathbf{k}\| = (\|\mathbf{v}\|^2 - \|\mathbf{l}\|^2)^{1/2}. \tag{6.7}$$

The theoretical time of hit is then

$$t_{i,\text{th}} = t_0 + \frac{1}{c}\left(\|\mathbf{l}\| - \frac{\|\mathbf{k}\|}{\tan\theta_C}\right) + \frac{\|\mathbf{k}\|}{v_g \sin\theta_C}, \tag{6.8}$$

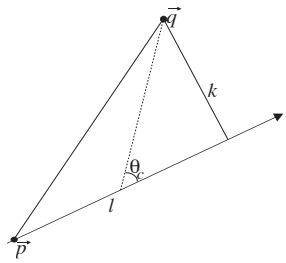

Figure 6.11: Geometry of the detection of a Čerenkov photon. A muon with direction **d** goes through point **p**. A Čerenkov photon is emitted at an angle θ_C and is detected by an OM located at **q**. The vector between **p** and **q** is **v**, and **k** is the vector towards **q** that is perpendicular to **d**. Figure reproduced from Heijboer (2004).

where v_g is the group velocity of light.

THE FIRST STAGE of track reconstruction is the linear prefit. Let us first denote the position of the i-th hit as (x_i, y_i, z_i). In the prefit it is assumed that the hits occur on points located on the muon track. This assumption can be a reasonable approximation if the length of the muon track in the detector is much larger than the attenuation length of light (Heijboer, 2004). The following relation thus holds:

$$\mathbf{y} = \mathbf{H\Theta}, \tag{6.9}$$

here $\mathbf{y}$ is a vector containing the hit positions,

$$\mathbf{y} = [x_1, y_1, z_1, \ldots, x_n], \tag{6.10}$$

$\mathbf{\Theta}$ is a vector containing the track parameters

$$\mathbf{\Theta} = [p_x, d_x, p_y, d_y, p_z, d_z]^T, \tag{6.11}$$

and $\mathbf{H}$ is a matrix containing the hit times

$$\mathbf{H} = \begin{pmatrix} 1 & ct_1 & 0 & 0 & 0 & 0 \\ 0 & 0 & 1 & ct_1 & 0 & 0 \\ 0 & 0 & 0 & 0 & 1 & ct_1 \\ 1 & ct_2 & 0 & 0 & 0 & 0 \\ 0 & 0 & 1 & ct_2 & 0 & 0 \\ \vdots & \vdots & \vdots & \vdots & \vdots & \vdots \\ 0 & 0 & 0 & 0 & 1 & ct_n \end{pmatrix}. \tag{6.12}$$

The estimate of the track parameters $\hat{\mathbf{\Theta}}$ can be calculated by minimizing the χ^2,

$$\chi^2 = [\mathbf{y} - \mathbf{H}\hat{\mathbf{\Theta}}]^T \mathbf{V}^{-1} [\mathbf{y} - \mathbf{H}\hat{\mathbf{\Theta}}], \tag{6.13}$$

where $\mathbf{V}$ is the covariance matrix of the error estimates on the hit positions, which usually is assumed to be diagonal. By minimizing χ^2 we can obtain

$$\hat{\mathbf{\Theta}} = [\mathbf{H}^T \mathbf{V}^{-1} \mathbf{H}]^{-1} \mathbf{H}^T \mathbf{V}^{-1} \mathbf{y}. \tag{6.14}$$

FOR THE SECOND STAGE, an M-estimator fit is performed. This fit works by maximising a function $g(r)$. The fit is not very sensitive

to the accuracy of the starting value, so it seems a logical continuation of the previous stage. The function of the time residuals r_i that provides good results are found to be

$$g(r_i) = -2\sqrt{1 + r_i^2/2} + 2. \tag{6.15}$$

The hits used in this stage are based on the result of the linear prefit. The time residual r_i must satisfy -150 ns $\leq r_i \leq 150$ ns and a distance from the fitted track no larger than 100 m.

THE THIRD STEP is a maximum-likelihood fit where the hit selection is based on the results of the M-estimator fit. The residuals used in this stage must satisfy $-0.5 \times R \leq R_i \leq R$, where R is the root mean square of the residuals used for the M-estimator fit. Hits that are part of a coincidence are also selected. The maximum-likelihood fit is performed by searching for parameters that maximize

$$P(\text{event}|\text{track}) = \prod_i P(t_i|t_{i,\text{th}}, a_i, b_i, A_i). \tag{6.16}$$

Here $P(t_i|t_{i,\text{th}}, a_i, b_i, A_i)$ is a probability distribution function (PDF) of t_i given $(t_{i,\text{th}}, a_i, b_i, A_i)$, where A_i is the amplitude of the hit, and

$$b_i = \frac{\|\mathbf{k}_i\|}{\sin\theta_C} \tag{6.17}$$

is the length of the photon path, and

$$a_i = [\mathbf{v} - \mathbf{d}\,(\|\mathbf{l}\| - b)] \cdot \mathbf{w} \tag{6.18}$$

is the cosine of the angle of incidence of the photon on the OM. Here $\mathbf{w}$ is the direction where the OM points. For a head-on collision of a photon with the photocathode, $a = -1$, whereas $a = 1$ means that the photon hits the insensitive rear of the OM.

The PDF used in this fit was developed by Hubaut (1999), and is shown in Figure 6.12. This PDF does not take photon hits due to backgrounds into account.

THE LAST TWO steps are then repeated with different starting points as input tracks. The different starting points are calculated

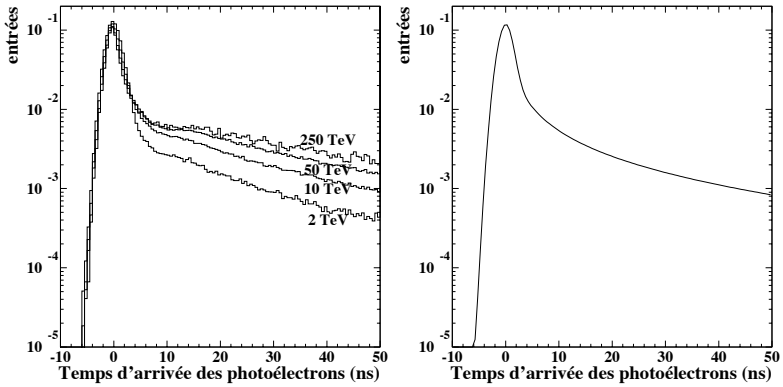

Figure 6.12: The shape of the PDF used in the maximum-likelihood. On the left is the PDF based on simulations, for Čerenkov photons coming from muons of different energies. On the right is a parametrisation of the PDF for a muon of energy 10 TeV. Figures reproduced from Hubaut (1999).

by performing a series of rotations and translations. The result with the best likelihood per degree of freedom is then kept. The number of starting points that result in track estimates compatible with the preferred result (those that give the same track direction to within 1°) is called N_{comp}.

THE FINAL STEP is then to use the starting point obtained from the previous step as a starting point for the maximum-likelihood fit with an improved PDF, which is the sum of the PDF for signal hits and optical background hits:

$$P(t_i|t_{i,\text{th}}, a_i, b_i, A_i). = \frac{1}{N_{\text{total}}}(P_{\text{sig}}N_{\text{sig}} + R_{\text{bg}}), \tag{6.19}$$

here N_{total} and N_{sig} are the total number of hits and the number of signal hits, and $R_{\text{bg}} = N_{\text{bg}}/\Delta t = N_{\text{bg}}P_{\text{bg}}$ is the optical background rate. Δt is the time window of the selection of hits in the event and N_{bg} is the expected number hits due to background. For this fit only hits with residuals between -250 ns and 250 ns and hits within local coincidences are used.

The final quality of the fit can be characterized by the quantity Λ which is defined to be

$$\Lambda \equiv \frac{\log L}{N_{\text{DOF}}} + 0.1(N_{\text{comp}} - 1), \tag{6.20}$$

where L is the likelihood at maximum and N_{DOF} is the degree of freedom. A higher Λ value means a better-reconstructed event.

The covariance matrix $\mathbf{V}$ can also be calculated by calculating the second derivatives of the likelihood function at the fitted maximum:

$$[\mathbf{V}^{-1}]_{ij} = -\frac{\partial^2 \log L}{\partial \mathbf{x}_i \partial \mathbf{x}_j}, \tag{6.21}$$

where $\mathbf{x} = (p_x, p_y, p_z, \theta, \phi)$. From this covariance matrix we can extract the covariance matrix for the reconstructed azimuth $\hat{\phi}$ and the reconstructed zenith distance $\hat{\theta}$:

$$\hat{\sigma} = \begin{bmatrix} \sigma_{\phi}^2 & \sigma_{\phi\theta} \\ \sigma_{\phi\theta} & \sigma_{\theta}^2 \end{bmatrix} \tag{6.22}$$

The error estimate of the direction of the reconstructed muon track σ_ψ can then be obtained from the covariance matrix, i.e.

$$\sigma_\psi = \left(\sin\hat{\theta}\sigma_{\phi}^2 + \sigma_{\theta}^2 + 2\sin\hat{\theta}\sigma_{\phi\theta} \right)^{1/2}. \tag{6.23}$$

These two parameters, Λ and σ_ψ, are often used for event selections. In later chapters these parameters will be used to evaluate the quality of the fit and as basis for cuts.

Knowing how the ANTARES telescope works and how muon tracks are reconstructed, we can then proceed to the simulations of downgoing muon events in order to investigate the sensitivity of the ANTARES telescope high-energy γ-rays.